# Energy Exchange Dynamics across L-H Transitions in NSTX

A. Diallo[1], S. Banerjee[2], S.J. Zweben[1] and T. Stoltzfus-Dueck[1]

[1]Princeton Plasma Physics Laboratory, Princeton University, Princeton, NJ, USA
[2]Institute for Plasma Research, Bhat, Gandhinagar 382428, Gujarat, India

*Corresponding author:* adiallo@pppl.gov

**Abstract:**
We studied the energy exchange dynamics across the low-to-high-confinement (L-H) in NSTX discharges using the gas-puff imaging (GPI). The investigation focused on the energy exchange between flows and turbulence, to help clarify the mechanism of the L-H transition. We apply this study to three type of heating schemes, including a total of 17 shots from the NSTX 2010 campaign run. Results show that the edge fluctuation characteristics (fluctuation levels, radial and poloidal correlation lengths) measured using GPI do not vary just prior to the H-mode transition, but change after the transition. Using a velocimetry approach (orthogonal-programming decomposition), velocity fields of a 24 $\times$ 30 cm GPI view during the L-H transition were obtained with good spatial ($\sim$1 cm) and temporal ($\sim$2.5 $\mu$s) resolutions. Analysis using these velocity fields shows that the production term, which is a proxy for the transfer of the energy from mean flows to turbulence or vice-versa, is systematically negative just prior to the L-H transition, which is inconsistent with the predator-prey paradigm. Using the inferred production term, an estimate of the L-H transition duration is found to be 25 ms, which is much larger than the measured duration. These discrepancies are further reinforced by consideration of the ratio between the kinetic energy in the mean flow to the thermal free energy, which is estimated to be much less than 1, which suggests that turbulence depletion mechanism may not be playing an important role in the transition to the H-mode. Although the Reynolds work is too small to directly deplete the turbulent free energy reservoir, order-of-magnitude analysis shows that the Reynolds stress may still make a non-negligible contribution to the observed poloidal flows.

## 1 Introduction

Since the discovery of the high confinement (referred to as H-mode) regime in the ASDEX tokamak [1, 2], it has become the standard mode of operation of present tokamaks and is planned for future fusion devices such as ITER. This H-mode is associated with the formation of an edge transport barrier that causes a transition from a low (L) to high (H) confinement regime resulting in improved performance (i.e., temperature, density, and energy confinement time). Operationally, the L-H transition occurs when the injected heat (beam, radio frequency waves, and/or ohmic) exceeds a threshold. The physics governing this transition is, however, unclear, and remains one of the open issues in fusion research.

Most theoretical descriptions of the L-H transition are based on the shear of the radial electric field and coincident $\mathbf{E} \times \mathbf{B}$ poloidal flow shear, which is thought to be responsible for the onset of the anomalous transport suppression [3]. First introduced by Ref. [4], it is generally supposed that stabilization of anomalous transport can be achieved by the flow shear via the breaking and/or distortion of edge turbulence eddies. Later, a self-consistent model of the L-H transition was derived from coupled nonlinear envelope equations for the fluctuation level and $E_r^{'}$ [5]. This derived model is a paradigm that is referred to as the predator-prey model. *The key point of this model is that there is nonlinear energy transfer from turbulence to flows via the Reynolds* *stress.This transfer drives a sheared zonal* $\mathbf{E}\times\mathbf{B}$ *flow, and concurrently directly depletes the turbulent fluctuations.* Alternatively, the contribution of $\nabla p_i$ to $E_r$ drives the sheared zonal E×B flows. Depending on the model, turbulence suppression is either due to direct depletion by the Reynolds-stress-induced energy transfer or due to the $\mathbf{E}\times\mathbf{B}$ shearing of eddies, which reduce the effective growth rate and increase the damping of the turbulent fluctuations. Overall, in the models described above, turbulence suppression is thought to trigger the L-H transition. Experimentally, several machines (EAST [6], DIII-D [7], C-Mod [8], and HL-2A [9]) have found that turbulence driven mean flows enhance the edge shear flow, which was thought to trigger the L-H transition, essentially consistent with the predator-prey paradigm. However, similar investigations of energy transfer between perpendicular flows and turbulence in the plasma boundary region of the JET tokamak (in ohmic and diverted discharges) have shown that the energy transfer from the zonal flows to turbulence can be both positive and negative in the proximity of sheared flows [10]. Although this work was not applied to the L-H transition, it suggests as an example that the turbulence can be either pumped or depleted by the sheared flows, pointing to possible ambiguity in using the energy transfer as a key mechanism in the studies. In this paper, we analyze the L-H transition dynamics on NSTX using the velocimetry of 2-D edge turbulence data from gas-puff imaging (GPI). More specifically, we describe turbulence correlation analyses and determine the velocity components at the edge across the L-H transition for 17 discharges with three types of heating power (neutral beam injection - NBI, ohmic, and radio frequency - RF). The turbulence dynamics are examined and the energy transfer between turbulence and mean flow is computed. Using a reduced model equation of edge flows and turbulence, the energy transfer dynamics is compared with the turbulence depletion hypothesis of the predator-prey model of the L-H transition.

## 2 Underlying model equations

Our analysis will rest on a *minimal model* of edge turbulence and sheared flows, using the very simple two-fluid flux-tube equations of Ref. [11], which make the following assumptions: isothermal electrons; a single species of singly-ionized cold ions; purely resistive parallel dynamics; frequencies fast relative to ion transit ($\omega \gg v_{ti}/qR$); and a shearless, simple-circular, large-aspect-ratio magnetic geometry. Although this model must be generalized for detailed quantitative calculations, it is adequate to capture the general structure and make order-of-magnitude predictions. In particular, one may relax any or all of the listed assumptions without changing the qualitative conclusions underlying our data analysis.

As shown in Ref. [11], our minimal model for edge turbulence nonlinearly conserves a free energy, whose evolution governs the rms amplitude of the turbulent fluctuations. We decompose this free energy into a thermal portion $E_n \doteq \int \mathrm{d}\mathcal{V}\,(T_{e0}/2n_0)n_e^2$, a nonzonal $\boldsymbol{E}\times\boldsymbol{B}$ portion $E_\sim \doteq \int \mathrm{d}\mathcal{V}\,\frac{1}{2}n_0 m_i[(\tilde{v}_E^y)^2 + (\tilde{v}_E^x)^2]$, and a zonal $\boldsymbol{E}\times\boldsymbol{B}$ portion $E_z \doteq \int \mathrm{d}\mathcal{V}\,\frac{1}{2}n_0 m_i\langle v_E^y\rangle^2$, with $x$ and $y$ the radial and binormal coordinates, $v_E^x \doteq \boldsymbol{v}_E\cdot\nabla x$ and $v_E^y \doteq \boldsymbol{v}_E\cdot\nabla y$ components of the $\boldsymbol{E}\times\boldsymbol{B}$ drift, $\int \mathrm{d}\mathcal{V}$ a volume integral, $\langle\cdots\rangle$ the flux surface average, and tildes indicating the nonzonal portion, e.g. $\tilde{v}_E^y \doteq v_E^y - \langle v_E^y\rangle$:

$$\partial_t E_n = T_{e0}\int \mathrm{d}\mathcal{V}\left[n_e v_E^x \frac{1}{L_n} - \phi\mathcal{K}\left(n_e\right) - \frac{1}{n_0 e} j_\parallel \nabla_\parallel n_e\right], \tag{1}$$

$$\partial_t E_\sim = \int \mathrm{d}\mathcal{V}[T_{e0}\tilde{\phi}\mathcal{K}(n_e) + j_\parallel\nabla_\parallel\phi - n_0 m_i(\tilde{v}_E^x\tilde{v}_E^y)\partial_x\left\langle v_E^y\right\rangle], \tag{2}$$

$$\partial_t E_z = \int \mathrm{d}\mathcal{V}[T_{e0}\langle\phi\rangle\mathcal{K}(n_e) + n_0 m_i(\tilde{v}_E^x\tilde{v}_E^y)\partial_x\left\langle v_E^y\right\rangle], \tag{3}$$

in which the curvature operator is defined as $\mathcal{K} \doteq -(2/B^2)\hat{\boldsymbol{b}} \times \nabla B \cdot \nabla$. Note that in Eqs. (1)–(3), we have discarded boundary terms. For detailed discussions about these equation, the reader is referred to Ref. [11].

In experimental investigations of energy balance across the L-H transition, it is important to retain Eq. (1) along with Eqs. (2) and (3), for the following reason: the parallel current $j_\parallel$ mediates an energy transfer between $E_n$ and $E_\sim$ on rapid electron transit timescales, acting until electrons approach adiabatic response. Since the Reynolds work $n_0 m_i (\tilde{v}_E^x \tilde{v}_E^y) \partial_x \langle v_E^y \rangle$ causes energy evolution on timescales much longer than electron transit, it cannot strongly change the ratio $E_\sim / E_{\tilde{n}}$. So, in order to directly suppress the turbulence, it must deplete the total turbulent energy $(E_{\tilde{n}} + E_\sim)$, which is approximately equal to $E_{\tilde{n}}$ for the typical edge turbulence case $k_\perp \rho_s \sim 0.1$. On timescales faster than poloidal rotation damping, this requires

$$\frac{E_z}{E_{\tilde{n}}} = \frac{\int \mathrm{d}\mathcal{V} \, \langle v_E^y \rangle^2 / c_s^2}{\int \mathrm{d}\mathcal{V} \, \tilde{n}_e^2 / n_0^2} \tag{4}$$

to be order unity, with $E_{\tilde{n}}$ evaluated immediately pre-transition and using the increase in $E_z$ over the transition. Since poloidal rotation is typically damped towards its neoclassical value at a rate of order the ion transit frequency $\nu \sim v_{ti}/qR$ [12, 13] the Reynolds stress contribution to the poloidal rotation may be very crudely estimated as $\langle v_E^y \rangle \sim -\nu^{-1} \partial_x \langle \tilde{v}_E^x \tilde{v}_E^y \rangle \sim -(qR/v_{ti}) \partial_x \langle \tilde{v}_E^x \tilde{v}_E^y \rangle$. Although this estimate is too rough for detailed quantitative comparison, it is adequate for an order-of-magnitude check.

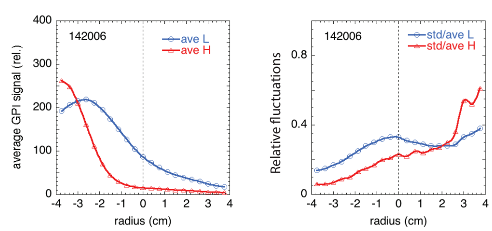


*FIG. 1: (Color online). (Color online). Radial profiles of the GPI signal (left panel) and its relative fluctuation level (right panel), averaged over the L and H-mode periods for the RF discharge 142006. The radial profiles change in response to rapid electron density and temperature changes at the transition. The relative fluctuation level decreases by about a factor-of-two inside and near the separatrix. The dashed line represents the separatrix.*

In principle, the flux surface average is a poloidal and toroidal average over an entire flux surface. However, since the gas-puff imaging (GPI) diagnostic only views (see Sec. 3 below for details) a small fraction of the surface, the poloidal spatial average over the GPI view is a poor approximation to the total flux-surface average. For this reason, we estimate the flux-surface average of GPI emission with a combination of a poloidal average (across the field of view) and a low-pass frequency filter (here, a cutoff at 1 kHz was used), exploiting a typical separation in frequency scales between the slow temporal evolution of the zonal component and the fast temporal evolution of the turbulent fluctuations.

# 3 Experimental Approach

Since gas-puff imaging is central to the analysis described below, we refer the reader to a more extensive description of the GPI diagnostics elsewhere [14, 15].

The directions $x$, $y$ labeled in the above section correspond, respectively, to radial $r$ and poloidal $\theta$ in the remainder of the text. For the study presented below, the collected images are processed to determine the spatial correlations (radial and poloidal lengths). Furthermore, these images are processed using velocimetry techniques to determine the velocity fields and to compute the various terms in the model equations highlighted in Sec 2 in order to test the L-H models.

Edge turbulence characteristics across L-H transitions in NSTX were described previously using GPI data taken in 2009 [16], and the present database from 2010 shows the same general characteristics. The most dramatic change at the L-H transition is a rapid reduction in relative GPI light fluctuation levels ($\tilde{I}/\bar{I}$) inside and near the separatrix, which occurs within $\sim 100\ \mu$s of the L-H transition time as seen in the standard $D_\alpha$ diagnostics. Examples the radial profiles of the GPI signal level and its relative fluctuation level just before and after the transition are shown in figure 1.

The time dependence of the relative GPI fluctuation level averaged over all 17 shots in the present database, at the location 1 cm inside the separatrix. These times are measured with respect to the time at which the GPI fluctuation level reaches the H-mode state in each shot, which has an uncertainty of about $\pm$ 0.1 ms. There is no significant time variation in the relative fluctuation level during the 3 ms preceding the transition, and the sudden drop at the transition from ($\tilde{I}/\bar{I}$ 25% to 15% occurs consistently over 0.1 msec. Note that the shot-to-shot variations during the L-mode period, are 4% in $\tilde{I}/\bar{I}$.

## Application of velocimetry to GPI

Edge turbulence characteristics across L-H transitions in NSTX were described previously using GPI data taken in 2009 [16], and the database from 2010 shows the same general characteristics. The most dramatic change at the L-H transition is a rapid reduction in relative GPI light fluctuation levels ($\tilde{I}/\bar{I}$) inside and near the separatrix ($\tilde{I}$ is the rms fluctuations and $\bar{I}$ is the mean intensity fluctuations of the GPI signal), which occurs within $\sim 100\ \mu$s of the L-H transition time as seen in the standard $D_\alpha$ diagnostics. Examples the radial profiles of the GPI signal level and its relative fluctuation level just before and after the transition are shown in figure 1.

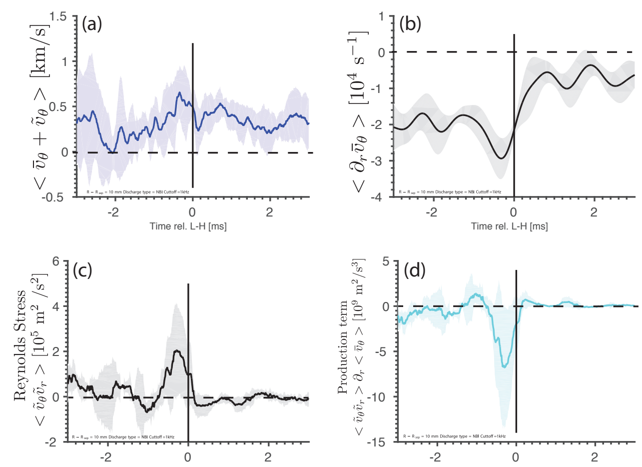


*FIG. 2: (Color online). NBI case: flows and derived quantities across the L-H transition. (a) Poloidal flow velocity containing both mean and fluctuating component. (b) The shear in the mean poloidal flow appears to increases across the L-H transition. (c) The Reynolds stress $< \tilde{v}_\theta \tilde{v}_r >$ peaks prior to the L-H transition. (d) The production term $< \tilde{v}_\theta \tilde{v}_r > \partial_r < \bar{v}_\theta >$ is negative during the L-H transition. The shaded area represents the standard deviation from all the NBI discharges.*

To evaluate the energy exchange dynamics using GPI, we use velocimetry to measure the local 2D turbulence motion, and assume that the turbulence motion is equivalent to the local

$\mathbf{E} \times \mathbf{B}$ fluid motion. This is a common assumption in the analysis of GPI [8], beam-emission-spectroscopy (BES) [17], and Doppler reflectometry diagnostics of edge turbulence [18], but is not rigorously true due to the possible turbulence phase velocity in the rest frame of the fluid [19]. There are also systematic limitations and uncertainties in any velocimetry analysis of GPI data, such as the well-known "barber-pole" effect, as discussed in [20]. Another source of uncertainty is the fact that velocimetry techniques show velocities to the intensity gradient. Therefore, velocities along isocontours of intensity are invisible. This is an unavoidable ambiguity that is shared by GPI velocimetry, BES velocimetry, and any other analogous techniques.

To extract the time varying 2D velocity field $\mathbf{v}(r, \theta, t)$ from the intensity fluctuations recorded with the GPI diagnostic, we use the orthogonal dynamic programming (ODP) technique. The ODP technique is described in detail in ref. [21]. This technique has the merit of determining the velocity field at the sampling time and with spatial resolution close to the images, which are advantages over the commonly used time-delay estimate (TDE) velocity estimates.

Probe measurements of the energy transfer represent a challenge, mainly due to the spatial undersampling of the region of interest. GPI offers more spatial points than probes do, reducing this challenge. Here, we compute the Reynolds stress ($< \tilde{v}_\theta \tilde{v}_r >$) and the production term ($< \tilde{v}_\theta \tilde{v}_r > \partial_r < \bar{v}_\theta >$) to qualitatively provide the energy transfer direction during L-H transition. The key metric is the energy transfer from mean flows to turbulence, which is directly related to the momentum flux and the radial gradient in the flow. This quantity can be either positive (turbulence to driven flows) or negative (energy transfer from DC flow to turbulence).

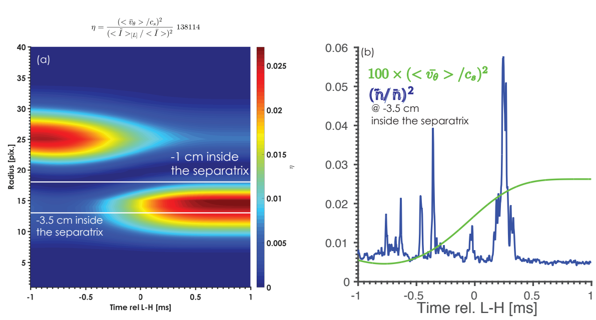


*FIG. 3: (Color online). NBI case. Energy ratio of the kinetic energy to the thermal free energy. (a) Radial profile as a function of the time relative to the L-H transition. (b) Time history at 3.5 cm inside the separatrix of the thermal free energy and 100 times the kinetic energy.*

## Energy transfer computations: Results

We have computed the 2D velocity data $\mathbf{v} = \bar{\mathbf{v}} + \tilde{\mathbf{v}}$, $\forall(r, \theta, t)$, where $r$ represents the major radius, $\theta$ describes the poloidal direction, and $t$ is the time. Figure 2 shows the flow velocities and derived parameters, namely, the poloidally averaged poloidal flow, its shear, the Reynolds stress, and the production terms, for the NBI heated discharges. In thisfigure, all these quantities are computed at radial position 1 cm inside the last closed flux surface. The shaded area in each panels around each solid line represents the standard deviations. The shear in poloidal flow generally increases after the L-H transition. Note that it is the absolute value of the shear that is responsible for shearing apart the eddies. For all heating schemes, the absolute shear velocity decreases across the L-H transition, which is inconsistent with the idea that flow shear is suppressing the turbulence as described in Ref. [4]. The inferred absolute shear velocity is inconsistent with the shear-flow model. However, GPI emission bands become narrow across the L-H transition and the fluctuation level drops across the L-H transition, in which case the possibility that the decrease in our inferred flow shear is an artifact cannot be ruled out.

Below, we show for one heating scheme (NBI) a test of the energy exchange dynamics across the L-H transition. First, we look at the exchange dynamic using the Reynolds stress and production terms. Figure 2 (c) & (d) display the Reynolds stress and production terms across the L-H transition at 1 cm inside the separatrix. In these figures, the Reynolds stress clearly decreases in H-mode. The peaking of the Reynolds stress is not systematic as for other heating schemes (not shown here), this peaking does not occur.

Further, contrary to expectations of the predator prey model's predictions, we systematically observe a negative production term just prior to the L-H transition, suggesting a transfer of energy from mean flows to turbulence. Despite the implication that shear flows are apparently exciting the turbulence, Fig. **??** shows the turbulence levels to drop across the L-H transition. These observations can only be reconciled if a different term in the energy balance equations becomes strongly negative at the L-H transition, overwhelming the Reynolds work to cause turbulence suppression.

To address the above point, we recall from Sec. 2 and Ref. [11] that for the energy transfer to mean flows to contribute significantly to the depletion of the turbulence the condition $\frac{\langle\bar{v}_\theta\rangle^2/c_s^2}{(\tilde{n}_e/n_{e0})^2} \gtrsim 1$ is required. Note that $(\tilde{n}_e/n_{e0})^2$ is that of the L-mode phase so that the ratio to be compared becomes $\eta \doteq \frac{\langle\bar{v}_\theta\rangle^2/c_s^2}{(<\tilde{I}^2>_{[L]}/\bar{I}^2)}$, where $(\tilde{n}_e/n_{e0}) \sim \tilde{I}/\bar{I}$, and $<\tilde{I}^2>_{[L]}^{1/2}$ is the rms of the GPI intensity fluctuations over the L-mode phase at a given radius. Figures 3(a) displays the 2D spatial profiles of energy ratio for the NBI heating schemes across the L-H transition. This figure shows that the kinetic energy in the mean flow (proportional to $\langle\bar{v}_\theta\rangle^2/c_s^2$) remains much smaller than the thermal free energy (proportional to $(\tilde{n}_e/n_{e0})^2$) even at radius 3.5 cm inside the LCFS, where the energy ratio takes its maximum. The two order magnitude difference in the energies substantiates the argument that the energy associated with the mean flow is unable to account for the depletion of the turbulence energy. As stated above the depletion is the fundamental aspect of the predator-prey model, resulting in a discrepancy with our data. In other words, the energy transfer due to Reynolds stress is not big enough to directly deplete the energy in the turbulence.

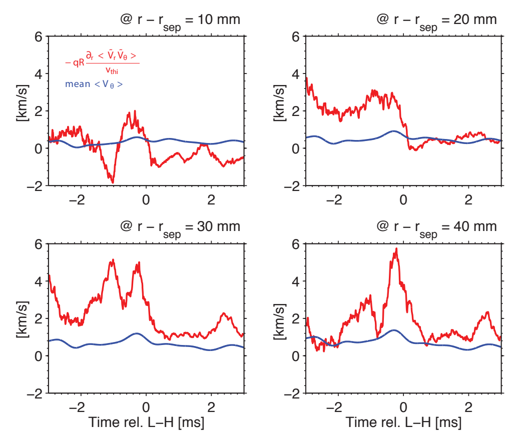


*FIG. 4: (Color online). NBI case: the comparison at various radii between the measured mean flow to the contribution of the Reynolds stress to the mean flow shows order of magnitude agreement (see text for discussion).*

Finally, we examine another way to test the depletion hypothesis by estimating how long would the L-H transition take given this production term. We refer to this production generated L-H transition time as $\tau^{RS}_{L-H}$. We estimate this by taking the ratio $\tau^{RS}_{L-H} = E_{\tilde{n}}/(n_0 m_i (<\tilde{v}_\theta \tilde{v}_r> \partial_r <\bar{v}_\theta>) \quad \Leftrightarrow \quad \tau^{RS}_{L-H} = 0.5 c_s^2 \left(\tilde{n}_e/n_{e0}\right)^2/(<\tilde{v}_\theta \tilde{v}_r> \partial_r <\bar{v}_\theta>)$, where $E_{\tilde{n}} \doteq (n_0 T_{e0}/2) \left(\tilde{n}/n_0\right)^2$. Assuming typical separatrix electron temperature $T_e \sim 60$eV, $(\tilde{n}_e/n_{e0})^2 \sim 0.1$, and the production term given by fig. 2(d) of about $5{\cdot}10^9$ m$^2$/s$^3$, we get a dimensional time indicating that the L-H transition duration $\tau^{RS}_{L-H}$ should be about 25 ms, which is far too long compared to the observed time of $\tau^{exp}_{L-H} \sim 100$ $\mu$s based on the fluctuations drop. This suggests that a much larger production term would be necessary to explain the typical L-H transition times.

Can the Reynolds stress contribute, however, to the mean flow itself? Here, we estimate the Reynolds-stress-driven flows and compare it to the measured mean flows. Under the assumptions highlighted in Sec. 2, one can crudely estimate the contribution of the Reynolds stress to the poloidal flow by estimating from experimental data $<\bar{v}_\theta>^{RS} \sim -qR\frac{\partial_r <\tilde{v}_\theta \tilde{v}_r>}{v_{this}}$, where $q$ is the safety factor, and $v_{this}$ is the ion thermal velocity. Figure 4 displays the estimated Reynolds stress contribution to the mean poloidal flow at four radii, which is compared with the GPI measured mean poloidal flow. This figure shows that both the Reynolds stress-driven mean flow (red curve) and the measured mean flow (blue curve) are of the same order of magnitude. This suggests that the contribution of the Reynolds stress to the mean flow cannot necessarily be discarded. [This is not inconsistent with the fact that Reynolds work is unable to deplete the turbulence free energy, since the turbulence free energy is much larger than the kinetic energy of the mean poloidal flows.] Note that given how crudely we estimate the contribution of the Reynolds stress, it is difficult to claim any consistency better than an order of magnitude.

# 4 Summary

We described detailed analyses of the energy dynamics during the L-H transition in NSTX over a database of 17 discharges spanning three heating schemes (NBI, ohmic, and RF), with only the NBI case shown here. These analyses relied on GPI data for determining the velocity fields. In addition, the analyses used a minimal model of edge turbulence and sheared flows to energy transfer from turbulence to flows via the Reynolds stress.

The relative GPI fluctuation decreased rapidly and consistently across the L-H transition, as shown in fig. 1, which is consistent with many previous experimental results at the L-H transition. However, there were no consistent changes *preceding* the L-H transition in the relative fluctuation level, the average poloidal or radial correlation lengths, the average poloidal or radial velocities, or the average poloidal flow shear. This absence of a precursor or trigger signal preceding the transition is also a relatively common result, but is shown here for NSTX in a clear way over a large database.

The analysis then proceeded to evaluate the energy exchange dynamics across the L-H transition based on the work of [8]. A new velocimetry approach, namely ODP, was applied to the GPI data for good spatial and temporal resolution of the velocity fields across the L-H transition. Given the radial and poloidal velocities, the Reynolds stress and production terms were estimated. It is observed that the production term is always negative just prior to the L-H transition, which suggests that energy is transferred from DC flow to turbulence. A negative production term is therefore inconsistent with the predator-prey model.Moreover, we further estimated how long would the L-H transition would take given the estimated production term and estimated a L-H transition duration of about 25 ms far too long compared to measurements. These discrepancies motivated theoretical work [11], which found that in order for Reynolds work to suppress the turbulence, it must deplete the total turbulent free energy. For this to occur, the increase in kinetic energy in the mean flow over the L-H transition must be comparable to the pre-transition thermal free energy. However, this ratio was found to be of order $10^{-2}$, even at its maximum (3.5cm inside the LCFS). The two order of magnitude difference suggests that this turbulence depletion mechanism is not key to the L-H transition, contrary to the predator-prey model. Non-negligible contribution to the poloidal flows by the Reynolds stress, however, is plausible given the comparable magnitude of the measured mean poloidal flows with the estimated Reynolds-stress-driven flows. Finally, we examine the turbulence hypothesis from multiple facets to show that given the caveats in the velocimetry analysis there seems to be evidence that suggest that turbulence depletion by Reynolds work is probably not the key mechanism in turbulence suppression at the L-H transition. In summary, this analysis suggests that turbulence depletion by Reynolds work is probably not the mechanism of the L-H transition in NSTX, but no alternative mechanism was found from either the experimental data or from a new model. However, there are significant uncertainties in the analysis and interpretation of the 2-D velocity fields derived from the GPI data, especially during the H-mode phase, which can be reduced with additional measurements and quantitative comparisons with turbulence simulations. This work is supported by U.S. Dept. of Energy contracts DE-AC02-09CH11466.

## References

[1] WAGNER, F., et al., Phys. Rev. Lett. **49** (1982) 1408.
[2] TEAM, A., Nuclear Fusion **29** (1989) 1959.
[3] BURRELL, K. H., Physics of Plasmas **4** (1997) 1499.
[4] BIGLARI, H., et al., Physics of Fluids B: Plasma Physics **2** (1990) 1.
[5] DIAMOND, P. H., et al., Phys. Rev. Lett. **72** (1994) 2565.
[6] XU, G., et al., Nuclear Fusion **54** (2014) 103002.
[7] YAN, Z., et al., Phys. Rev. Lett. **112** (2014) 125002.
[8] CZIEGLER, I., et al., Plasma Physics and Controlled Fusion **56** (2014) 075013.
[9] XU, M., et al., Phys. Rev. Lett. **108** (2012) 245001.
[10] SÁNCHEZ, E., et al., Journal of Nuclear Materials **337–339** (2005) 296 , PSI-16.
[11] STOLTZFUS-DUECK, T., Phys. of Plasmas **23** (2016) 054505.
[12] NOVAKOVSKII, S. V., et al., Phys. of Plasmas **4** (1997) 4272.
[13] SCOTT, B. D., New Journal of Physics **7** (2005) 92.
[14] ZWEBEN, et al., Phys. of Plasmas **13** (2006) 056114.
[15] ZWEBEN, S., et al., Nuclear Fusion **44** (2004) 134.
[16] ZWEBEN, S. J., et al., Phys. of Plasmas **17** (2010)102502.
[17] MCKEE, G. R., et al., Review of Scientific Instruments **77** (2006) 10F104.
[18] HIRSCH, M., et al., Plasma Physics and Controlled Fusion **43** (2001) 1641.
[19] MYRA, J., et al., Nuclear Fusion **53** (2013) 073013.
[20] SIERCHIO, J. M., et al., Review of Scientific Instruments **87** (2016) 023502.
[21] BANERJEE, S., et al., Review of Scientific Instruments **86** (2015) 033505.